

Nondilute effects reshape miscible displacement in porous media

Fei Yu ^{1,*}, Yandong Zhang ^{1,*}, Shuai Zheng ¹, Dongxiao Zhang ^{1,2} and Ke Xu ^{1,†}¹*Department of Energy and Resources Engineering, College of Engineering, Peking University, Beijing 100871, China*²*School of Environmental Science and Engineering, Southern University of Science and Technology, Shenzhen 518055, China*

(Received 3 August 2022; accepted 14 March 2023; published 19 April 2023)

Miscible displacement of nondilute fluid pairs in subsurface porous media plays a key role in CO₂ subsurface sequestration and many other applications. We conduct microfluidic experiments in a near-fracture porous geometry so that nondilute effects are isolated from other disruptive behaviors. We show that although Darcy-Fickian coupling works well for dilute fluid systems, it completely fails to predict nondilute fluid-fluid displacement. Compared to that predicted by Darcy-Fickian models, nondilute fluid-fluid displacement demonstrates much faster and “diffusive” mixing, an unexpected wedgelike mixing front, and abnormal convection perpendicular to the major concentration. Simply correcting Fick’s law cannot reproduce these phenomena. Maxwell-Stefan drifting and Korteweg stress may rationalize experimental observations, but major challenges emerge in microscopic modeling and upscaling. We provide this work as a benchmark and call for future study to incorporate appropriate nondilute effect terms at different scales into the modeling of CO₂ sequestration and other relevant applications.

DOI: [10.1103/PhysRevFluids.8.044501](https://doi.org/10.1103/PhysRevFluids.8.044501)

I. INTRODUCTION

CO₂ subsurface sequestration is considered as an effective strategy to reduce greenhouse gas emissions [1]. Saline aquifers and depleted hydrocarbon reservoirs are considered as feasible technology deployment options [2]. In both scenarios, mixing between the injected fluid and formation fluid in subsurface porous media largely determines the effectiveness of CO₂ storage [3].

At present, mass transfer in porous media is mostly modeled by coupling Darcy’s law of flow and Fick’s law of diffusion (dispersion) [4,5]. This Darcy-Fickian coupling has been widely adopted in studying fluid behaviors during CO₂ injection into saline aquifer layers or oil formations [6–8].

However, Fick’s law presupposes a dilute system [9], which is highly questionable in typical CO₂ sequestration practices. For example, in some deep saline aquifers with rich sodium and potassium ions [10–12], the contact of CO₂ with formation water may result in 30% or even higher bicarbonate concentration contrast. In depleted oil reservoirs, CO₂ and crude oil can be completely miscible which leads to 100% CO₂ concentration contrast [13,14], and the local concentration gradient can be as intensive as 40% per millimeter at the displacement fronts [15]. In these nondilute scenarios with high concentration and intensive concentration gradient, the applicability of Darcy-Fickian coupling is not guaranteed [9,16].

Microscopically, many unique phenomena in nondilute fluid systems have been reported, such as anomalous mixing of a single miscible droplet [17,18], and intensive local convection that is not

*These authors contributed equally to this work.

†kexu1989@pku.edu.cn

expected in a dilute system [17,19–21]. Thereafter, many researchers attempt to develop theoretical and numerical models to rationalize these nondilute effects. On anomalous diffusion, the standard Fickian dispersion model is expanded by a Taylor series to account for nonideal dispersion [22,23], and some adopt thermodynamically constrained averaging theory (TCAT) [16] that reformulates the diffusion driving force from concentration gradient to chemical activity or chemical potential gradient, based on which a wider mixing zone (thus stronger mixing) is predicted [24]. On convection induced by nondilute mixing, Maxwell-Stefan effects (a description of diffusion in multicomponent systems) [25,26] and Korteweg stress (an effective interfacial tension due to uneven concentration) [27,28] are introduced in the convection-diffusion equation, for diffusion-induced stress parallel [29] and perpendicular [17,30,31] to the concentration gradient, respectively.

At the scale of porous media, many clues of nondilute effects have also been identified during fluid-fluid displacement for CO₂ sequestration or hydrocarbon recovery applications [15,32]. Unfortunately, due to the unfavorable viscosity ratio or density ratio in these applications, nondilute effects in porous media flow are always accompanied with hydrodynamic instability (viscous fingering, Rayleigh-Darcy instability, etc.) [18,33] which can hardly be independently confirmed and quantified. The exact role of nondilute effects in miscible fluid-fluid displacement is thus still unclear, making it challenging to establish rigorous modeling methods in porous media.

In this paper, we isolate nondilute effects in porous media from other hydrodynamic instability during miscible fluid-fluid displacement, using microfluidic experiments and numerical simulation. We confirm that the nondilute effects are nontrivial and fundamentally reshape the mixing kinetics, and discuss in detail anomalous phenomena in nondilute fluid-fluid displacement. The goals of this paper are (1) to highlight the necessity to consider nondilute effects in modeling CO₂ sequestration or other nondilute miscible displacement in porous media, and (2) to preliminarily discuss possible strategies to incorporate nondilute effects in modeling. This work also provides an experimental benchmark for future investigation.

II. METHODS AND SETUP

A. Methodology

Microfluidic experiments, numerical simulations adopting Darcy-Fickian coupling, and theoretical solutions are compared to identify the role of nondilute effects during mixing in porous media, following these steps:

- 1) First, we check the reproducibility of microfluidic experiments, by conducting experiments using dilute fluid systems and compare experimental results with Darcy-Fickian simulation as well as in analytical solution. Their good matching is the premise of further investigations.
- 2) We then check whether good matching still holds for nondilute fluid pairs under the same flow conditions. If the matching is still good, we conclude that the nondilute effect may be trivial in practice; otherwise, we can attribute the differences to nondilute effects.
- 3) In the case that nondilute effects make a major difference, we will record microscopic and macroscopic behaviors that are unique to nondilute systems and then preliminarily explore possible solutions to address these effects in modeling.

B. Fluid systems

We carefully choose the fluid systems at ambient pressure and temperature for better emulating the miscibility and viscosity contrast of fluids involved in subsurface CO₂ sequestration. Components and properties of experimental fluid pairs are listed in Table I.

In this work, we call a fluid pair “dilute” if two fluids share >80 wt% of the same major component (solvent); in contrast, we choose the term “nondilute” fluid pair if there are two miscible fluids with no shared components (i.e., 100% concentration contrast). We define λ as the viscosity of the defending fluid over the viscosity of the invading fluid, and we choose fluid pairs with identical viscosity ($\lambda = 1$) for simplicity, and “with viscosity contrast” ($\lambda > 10$) to mimic CO₂ sequestration

TABLE I. Components and properties of fluid pairs used in the experiments.

System number	Features	Invading fluid	Invading fluid viscosity (mPa s)	Defending fluid	Defending fluid viscosity (mPa s)
1	Dilute $\lambda = 1^a$	Tetradecane +dye (0.06%)	2.0	Tetradecane	2.0
2	Dilute $\lambda \gg 1$	Liquid paraffin (80%)+heptane (20%)	19	Liquid paraffin	230
3	Nondilute $\lambda = 1$	N-butyl alcohol (88%) +heptane (12%)	2.1	Tetradecane	2.0
4	Nondilute $\lambda \gg 1$	Tetradecane	2.0	Liquid paraffin	230

^a λ is the viscosity ratio of the defending fluid and invading fluid.

where CO_2 is much less viscous than the formation fluids. The invading fluid was dyed with Sudan III (0.06 wt %), so we can visually track the sweep front development [34].

C. Experimental setup and procedure

We designed a near-fracture porous media model consisting of a highly conductive fracture and porous matrix as shown in Fig. 1(a). The porous matrix is exposed to the fracture at one side, and the other three boundaries are closed for simplicity. The porous matrix contains an array of cylindrical posts. The diameter of the posts is 1 mm; the pore-throat width (w) is 0.5 mm; depth is 1 mm; the fabrication accuracy is 0.1 mm. The permeability of the fracture is one order of magnitude higher than the porous matrix. The microfluidic experiment platform is shown in Fig. 1(b); it mainly consists of the micromodel, a syringe pump (LSP02-2B), a DV camera, and a LED lamp. The micromodel is horizontally positioned so gravitational effects can be neglected.

To minimize the effect of viscous fingering and highlight the nondilute effects, we first saturate the microfluidic model with the defending fluid and then inject the invading fluid into the fracture. The invading fluid first displaces the defending fluid in the conductive fracture within a very short time, and then gradually displaces and mixes with the defending fluid in the porous matrix. In this way, viscous fingering is limited at the very beginning of fluid-fluid displacement along the fracture, and cannot develop in the porous matrix. In addition, this design also restores extremely fractured

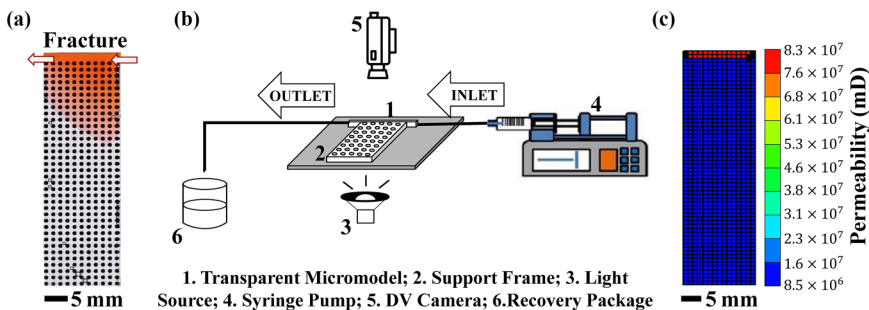


FIG. 1. Schematic illustration of the microfluidic model and experimental setup. (a) An image on the micromodel captured during an experiment. (b) The microfluidic platform setup. (c) The CMG simulation setup as the digital twin of the microfluidic experiment.

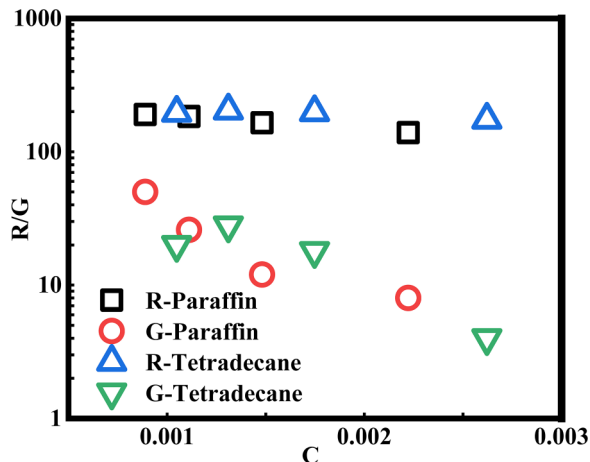


FIG. 2. The concentration-chromaticity data for tetradecane and paraffin. “R” represents the red channel, and “G” represents the green channel. Good matching can be identified.

reservoirs in CO₂ sequestration scenarios like depleted hydrocarbon reservoirs and other fractured media [35,36].

D. Numerical and theoretical solutions

We establish “digital twins” of microfluidic experiments using CMG software which adopts Darcy-Fickian coupling. We choose the diffusion coefficient as $D = 1.2 \times 10^{-9} \text{ m}^2/\text{s}$ [37,38], while CMG simulation shows that the displacement kinetics is insensitive to the value of D under high Péclet number ($Pe = \frac{u_f L_f}{D}$ where u_f , L_f , and D are the equivalent velocity in the fracture, the length of the fracture, and the diffusion coefficient, respectively). In addition, for cases $Pe \gg 1$, we adopt a complex potential theory which provides an analytical solution of displacement kinetics, shown in the Supplemental Material [39]. See the Supplemental Material [39] for detailed setup and derivation.

E. Image processing and quantification

We assume that the dye flows and diffuses along with the invading fluid, as also adopted by previous works [40,41]. The concentration profile can thus be quantified by resolving the dye concentration using the Beer-Lambert law [42]. This assumption is supported by our measurement of RGB values of tetradecane and paraffin with different Sudan III concentration under the same background light intensity, where we show that the concentration-chromaticity curves (Fig. 2) have little difference between the absorbance of tetradecane and paraffin. Therefore, in the experiment of cases 1–4, we chose to calibrate the invading fluid with the same dye concentration for different systems.

We define the line of the maximum dye color gradient as the displacement front, and accordingly define the relative sweep efficiency S as the ratio of the swept volume over total pore volume (V_P).

III. DEMONSTRATION OF MIXING KINETICS AND FLOW PATTERNS

In the demonstrative cases, the injection rate is fixed at 1 ml/min, corresponding to $Pe = 1.0 \times 10^5$, which is a typical value in CO₂ sequestration [43]. Results of dilute and nondilute fluid systems with $\lambda = 1$ and $\lambda \gg 1$ are compared. All experiments are reproducible as shown in the Supplemental Material [39].

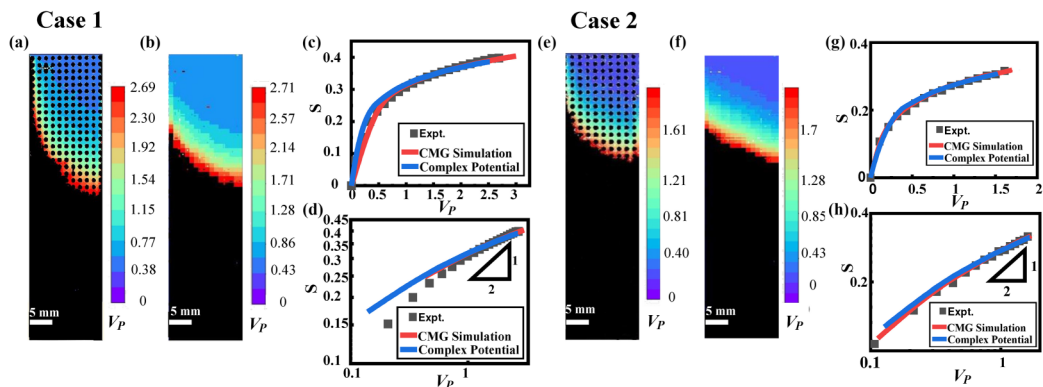


FIG. 3. Demonstrative results for dilute fluid systems. (a)–(d) Experimental and simulation results for case 1, including the comparison of S evolution in (a) experiment and (b) CMG simulation, where the color represents the position of the mixing front at certain injected V_p ; and the evolution of S with V_p in (c) ordinary coordinates and (d) log-log scale. (e)–(h) The experimental result of mixing front evolution, the CMG simulation of mixing front evolution, and the S - V_p plots in ordinary coordinates and log-log scale, correspondingly for case 2.

A. Displacement with dilute solution

We first investigate dilute systems, where Fick’s law is expected to hold. Fluid system 1 (dilute, $\lambda = 1$) is applied in case 1 and fluid system 2 (dilute, $\lambda \gg 1$) is applied in case 2. The development of the displacement front in the two experiments and corresponding CMG simulation, as well as the experimental, simulated, and analytical S - V_p correlations are shown in Fig. 3.

In both dilute cases, the displacement front is mildly inclined which is well predicted by Darcy-Fickian simulation and complex potential analytical solution. Except for minor mismatch at the very early stage (discussed in the Supplemental Material [39]), numerical simulation and complex potential theory well predict the experimentally measured S evolution with V_p , as shown in Figs. 3(c) and 3(g). In addition, as shown in a log-log plot of Figs. 3(d) and 3(h), S - V_p demonstrates subdiffusive kinetics, that S enlarges much slower than $V_p^{1/2}$.

We thus confirm that classic Darcy-Fickian coupling is valid for dilute miscible displacement, regardless of viscosity contrast. This good matching also proves that our experimental setup is physically reliable.

B. Displacement with nondilute solution

We then look into the miscible displacement of nondilute fluid pairs. Fluid system 3 (nondilute, $\lambda = 1$) is applied in case 3 and fluid system 4 (nondilute, $\lambda \gg 1$) is applied in case 4. The development of the displacement front in the two experiments and corresponding CMG simulation, as well as the experimental, simulated, and analytical S - V_p correlations are shown in Fig. 4.

A qualitative difference between experiments and simulation is identified, regardless of viscosity contrast. As shown in Figs. 4(a) and 4(e), the displacement front is wedgelike in the experiments, distinct from that of nondilute fluids and that predicted by the numerical simulation. Surprisingly, as shown in Figs. 4(d) and 4(h), a nice diffusive scaling ($S \sim V_p^{1/2}$) is experimentally observed, which is much faster than the subdiffusive scaling predicted by Darcy-Fickian coupling.

C. Microscopic observation of convection mode

We conduct microscopic characterization of local fluid flow when the mixing front sweeps through as illustrated in Fig. 5. We measure the velocities of impurities (u_{local} , discussed in the Supplemental Material [39]) to characterize the streamlines as shown in Figs. 5(b), 5(d), and 5(f).

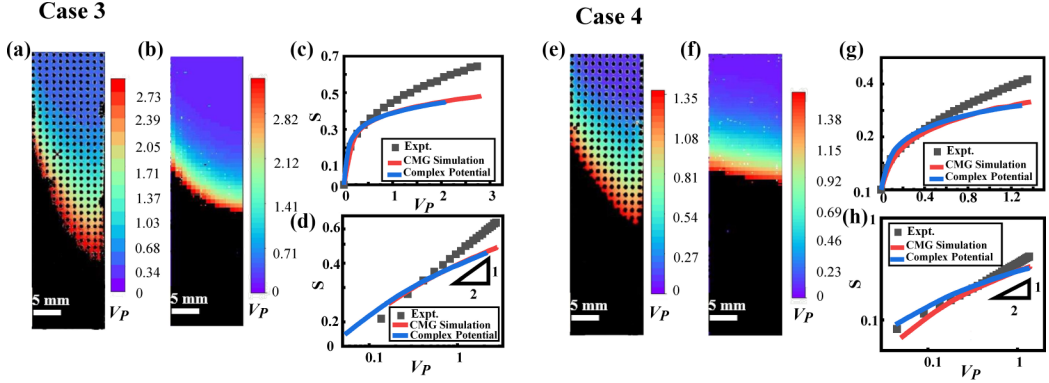


FIG. 4. Demonstrative results for nondilute fluid systems. (a)–(d) The experimental results of mixing front evolution, the CMG simulation of mixing front evolution, and the S - V_p plots in ordinary coordinates and in log-log scale, correspondingly for case 3. (e)–(h) The experimental result of mixing front evolution, the CMG simulation of mixing front evolution, and the S - V_p plots in ordinary coordinates and log-log scale, correspondingly for case 4.

We define the local Péclet number as $Pe_{\text{local}} = \frac{u_{\text{local}} w}{D}$ and compare the measured Pe_{local} with that at the same position and time in CMG simulation.

Figure 5(g) shows the results for case 1 (nondilute, $\lambda = 1$) and case 3 (nondilute, $\lambda = 1$). We note that Darcy-Fickian coupling predicts a time-independent velocity field under constant injection rate when $\lambda = 1$. CMG simulation well predicts the local velocity of case 1, while the Pe_{local} is two times larger than the CMG simulation for case 3.

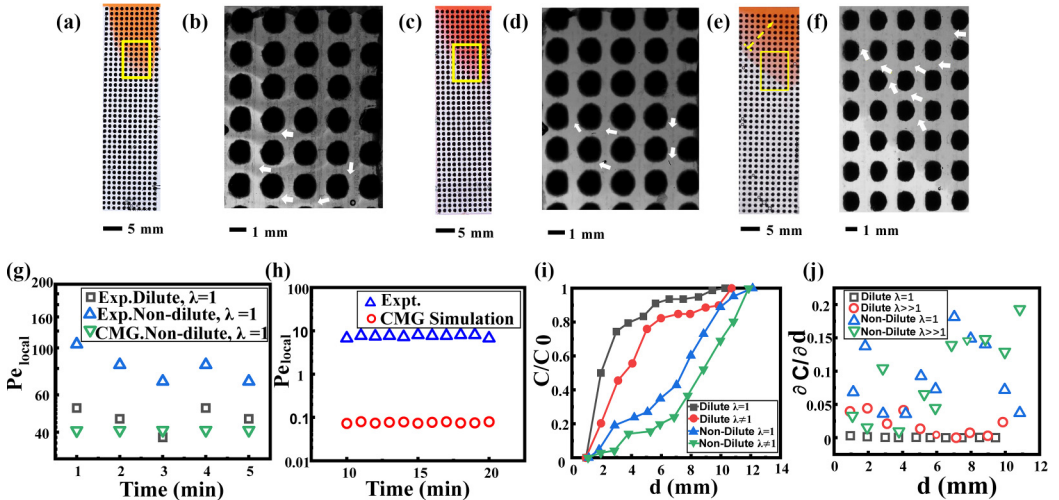


FIG. 5. Microscopic velocity measurement region (yellow rectangle) for (a) case 1; (c) case 3; (e) case 4 at $S = 0.28$. The direction of concentration profile measurement (yellow arrow) in the entire microfluidic model is shown in (e). (b), (d), (f) The microscopic characterization of local flow at 1min for case 1 and 3; 10 min for case 4 after fluid injection. The arrows represent the position of the dye impurity particles and the direction of the instantaneous velocity. Local Pe of the displacement front from experimental measurement and from CMG simulation for (g) cases 1 and 3; (h) case 4. (i) Normalized dye concentration distribution in the mixing zone. (j) Gradient of invading fluid concentration along the mixing zone.

TABLE II. Comparison of four cases.

	Dilute (cases 1 and 2)	Nondilute (cases 3 and 4)
Darcy-Fickian coupling	Valid	Not valid
S - V_p correlation	Subdiffusive	Diffusive
Mixing front morphology	Slightly inclined	Wedgelike
Convection at front	Weak	Intensive and perpendicular to concentration front
Mixing zone width	One to two pores	Approximately ten pores

Figure 5(h) shows the results in case 4 (nondilute, $\lambda \gg 1$), where the measured Pe_{local} 's are two orders of magnitude larger than those predicted by CMG simulation. In experiments, $Pe_{\text{local}} \sim 10$ so convection dominates over Fickian diffusion, while CMG simulation predicts $Pe_{\text{local}} < 0.1$ so molecular diffusion dominates over convection.

More surprisingly, the experimentally measured fluid velocity is statistically perpendicular to the front evolutionary direction (tangent to the front), without turbulence or circulation. As this convection is not predicted by Darcy-Fickian modeling, the driving force must be unique for nondilute systems. Original data and more details are shown in the Supplemental Material [39].

D. Mixing zone

We quantify the mixing zone behind the displacement front by measuring the chromaticity ratio between a position behind the displacement front and the injection position, for all four cases. We record the variation of normalized dye concentration (C/C_0 ; C_0 is the dye concentration of pure invading fluid) along the perpendicular direction of the displacement front at the moment of $S = 0.28$ for all cases as shown in Fig. 5(i). For both dilute and nondilute cases, the mixing zone is slightly wider in $\lambda \gg 1$ cases than in $\lambda = 1$ cases, which is rationalized by the enhanced mechanical dispersion due to viscous fingering. More importantly, the mixing zone of the nondilute displacement is remarkably wider than that of the dilute solutions.

We further calculate the concentration gradient profile along the mixing zones in all four cases. As shown in Fig. 5(j), the maximum concentration gradients in nondilute systems are at least one order of magnitude larger than the peak concentration gradients in the dilute systems.

E. Comparison of four comparative experiments

After successfully isolating the nondilute effect during miscible fluid-fluid displacement, we show that classic Darcy-Fickian coupling well predicts dilute displacement, but fails in predicting nondilute displacement, in both macroscopic mixing kinetics and microscopic flow features.

For nondilute system, wedgelike front morphology and much faster sweeping kinetics ($V_p^{1/2}$) are observed, regardless of the viscosity ratio. The nondilute fluid systems show much stronger convection at the mixing front that is perpendicular to the concentration gradient, and present a much wider mixing zone than dilute systems. Clearly, the nondilute effect significantly reshapes the displacement kinetics. A brief summary comparison of four cases is shown in Table II.

IV. PRELIMINARY EFFORTS TO ADDRESS NONDILUTE EFFECTS

We have confirmed that nondilute displacements show distinct kinetics from that of Darcy-Fickian displacement in dilute systems. In this section, we preliminarily discuss some possible strategies to address these nontrivial changes brought by nondilute effects in theoretical and numerical modeling.

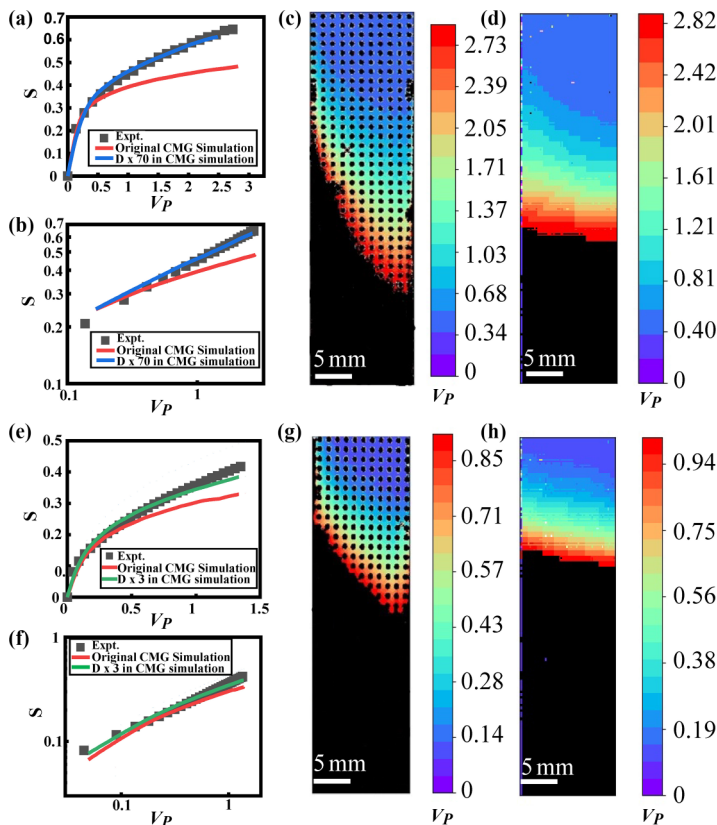


FIG. 6. Fitting diffusion coefficient to match demonstrative experiments of nondilute systems. For case 3: the S - V_P correlation when the diffusion coefficient is extended by 70 times (a) in ordinary coordinates and (b) in log-log scale. The flow pattern at the same S in (c) experiment; (d) CMG simulation. For case 4: the S - V_P correlation when the diffusion coefficient is extended by three times (e) in ordinary coordinates and (f) in log-log scale. The flow pattern of the nondilute solution with viscosity contrast at the same S in (g) experiment; (h) CMG simulation when the diffusion coefficient is increased by a factor of 3.

A. Correcting Fick's law

An intuitive idea to address the nondilute effect that may reproduce the enlarged mixing zone is simply assigning a much larger diffusion (dispersion) coefficient within the classic Darcy-Fickian framework. A superficially satisfactory fitting in sweep area evolution can be achieved when we amplify the diffusion coefficient by 70 times in case 3, as shown in Fig. 6. However, it fails in reproducing the wedgelike displacement front morphology, as demonstrated in Figs. 6(c) and 6(d). The convection at the front is also not predicted. We then fit the diffusion coefficient in the nondilute displacement with viscosity contrast (case 4), but we can neither get a satisfactory fitting for the S - V_P curve [Fig. 6(e)], nor qualitatively reproduce the displacement front morphology [Figs. 6(g) and 6(h)].

This missing of near-front convection and the mismatching of front morphology are still expected to hold if we simply replace Fick's law by nonlinear Fickian models, where the diffusion coefficient becomes a function of concentration [23], or the driving force is reformulated into other thermodynamic functionals than the concentration gradient [16]. To reproduce the local convection near the front, one or more concentration-correlated stress terms should be incorporated into the convection-diffusion equation.

B. Incorporating Maxwell-Stefan drifting

Maxwell-Stefan theory [29,44] suggests that unbalanced countercurrent diffusion flux of two components can induce convection. It provides an explanation of the thicker mixing zone as this countercurrent flux enhances local mixing capacity.

However, this drifting effect is expected to be parallel to the major concentration gradient, while experiments mainly show convection perpendicular to it. Therefore, the Maxwell-Stefan effect is not adequate to rationalize the experimental observation of convection direction.

C. Incorporating Korteweg stress

Incorporating Korteweg stress (effective interfacial tension) provides a solution to introduce the convection perpendicular to the concentration gradient at the mixing front, as Korteweg stress is positively correlated to the concentration gradient ($\Gamma_e = \kappa(\nabla C)^2$ [45]), and is perpendicular to the concentration gradient.

We note that the mixing zone is thinner near the outlet, and thicker upstream, as observed experimentally. Korteweg stress is thus larger in the downstream area than upstream. That is, spatially nonuniform Korteweg stress would drive flow along the front towards the downstream area, similar to the ‘‘Marangoni effect’’ in an immiscible system [46,47]. It thus rationalizes the origin of convection near the mixing interface far from the fracture that is along the mixing front pointing downstream.

Nevertheless, the physics of Korteweg stress is still under debate [27,28] and the relevant modeling approach is still challenging [45,48,49]. Deeper investigation, not only in fluid-fluid displacement dynamics, but also in Korteweg stress’s physical nature, should be conducted before we can confidently incorporate it into REV (representative elementary volume) scale modeling.

D. Summary of strategies to address nondilute effects

Maxwell-Stefan drifting can rationalize the thicker mixing zone, as the countercurrent convection enhances local mixing efficiency. Korteweg stress can rationalize the convection direction near the front, as the spatially nonuniform concentration gradient results in a driving force towards the downstream area along the mixing front. Correcting Fick’s law and the diffusion coefficient may help in quantitatively improving the accuracy but we cannot see its contribution in qualitatively explaining observed unique phenomena in nondilute systems.

V. DECAYING NONDILUTE EFFECTS UNDER DECREASING Pe

As both Maxwell-Stefan drifting and Korteweg stress are controlled by concentration gradient (∇C) rather than absolute concentration (C), this infers that reducing ∇C should dramatically weaken the deviation from Darcy-Fickian coupling, even without change of absolute concentration contrast.

One way to test this inference is to reduce Pe in experiments using a nondilute fluid pair and to observe how the deviation between experimental mixing kinetics and Darcy-Fickian simulation changes. As Pe decreases, the diffusion term gradually dominates over the convection term in the convection-diffusion equation, which flattens the concentration field near the front, thus reducing ∇C .

We thus conducted one more set of experiments using the same fluid system (system 4) but under different Pe (1.0×10^5 , 1.0×10^3 , 4.2). The development of the displacement front in the three experiments, in CMG simulation, and $S-V_p$ correlation with double log coordinates is shown in Fig. 7.

When $Pe \sim 10^5$, the experimental results well reproduce that shown in Figs. 7(a)–7(d), where a qualitative difference in $S-V_p$ scaling can be identified between experiment and Darcy-Fickian

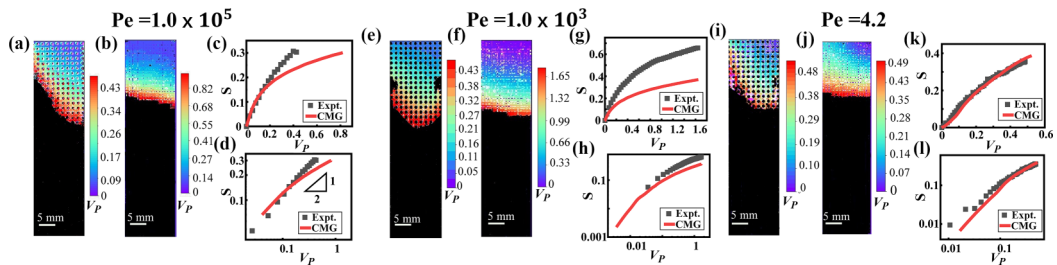


FIG. 7. Effects of Pe value on nondilute effect using system 4 (nondilute with viscosity contrast). $Pe \sim 10^5$: flow patterns at the same $S = 0.28$ in (a) experiment and in (b) CMG simulation. The S - V_p correlation in (c) in ordinary coordinates and in (d) log-log scale. $Pe \sim 10^3$: flow patterns at the same S in (e) experiment; (f) CMG simulation. The S - V_p correlation in (g) ordinary coordinates and in (h) log-log scale. $Pe \sim 1$: low patterns at the same S in (i) experiment and in (j) CMG simulation. The S - V_p correlation in (k) ordinary coordinates and in (l) log-log scale.

coupling: the experiment maintains $S \sim V_p^{1/2}$, while the simulation shows that S evolves much slower than $S \sim V_p^{1/2}$.

As Pe decreases, the difference between experiments and Darcy-Fickian simulations narrows. When Pe is small enough ($Pe = 4.2$), the experiment and simulation have already shown good agreement on both the displacement pattern and the $S \sim V_p$ relationship.

VI. LIMITATIONS AND IMPLICATIONS

Although the nondilute effect's nontrivial role is successfully demonstrated in this paper, still many detailed scientific problems are unclear. The exact conditions (concentrations, chemicals, flow conditions, etc.) for nondilute effects to be significant are still an open question.

Numerical methods to model Maxwell-Stefan drifting and Korteweg stress into mixing in porous media are still very challenging, not only because of the under-debate exact physical formulas and the unknown value of parameters in the Korteweg stress term, but also the difficulty in upscaling. High concentration gradient, which is the origin of the Maxwell-Stefan drifting and Korteweg stress, is microscopic and local, which is always confined in subpore geometry. It thus cannot be directly captured in large grids for upscaled simulation. For Maxwell-Stefan drifting, correcting the mechanical dispersion term may be a valid method; for Korteweg stress, some substitution models should be introduced on a larger scale.

In addition, our experiments are highly simplified compared to practical CO_2 sequestration. In a real sequestration scenario, dissolving of CO_2 may result in other nonclassic effects such as defending fluid swelling [50], thermal effect [51], and chemical reactions [52], and future work is required to incorporate these effects into consideration.

Nevertheless, we note that our presented experiments are using a very simple and easy to reproduce setup, with robust phenomena and well-quantified visualized data provided. The reproducibility has been supported by repeated experiments as shown in Sec. 6 of the Supplemental Material [39]. Our experiments thus can be applied as a benchmark for future investigation of nondilute mixing in porous media.

VII. CONCLUSION

We highlight the necessity of incorporating nondilute effects into the modeling of miscible displacement and mixing in porous media, by experimentally isolating nondilute effects and illustrating their nontrivial impacts on miscible displacement and mixing.

Nondilute effects largely enhance the mixing efficiency, resulting in a distinct wedgelike displacement front and diffusive displacement kinetics in a near-fracture porous medium. During nondilute displacement and mixing in the experiments, strong convection emerges near the displacement front. This local convection is perpendicular to the major concentration gradient. Macroscopic observation identifies a much thicker mixing zone in nondilute displacement than in dilute displacement. All the above observations cannot be rationalized in the framework of classic Darcy-Fickian coupling.

We compare some preliminary strategies to address nondilute effects in modeling, and conclude that simply correcting Fick's law or considering the drifting effect are not adequate. Among many reported mechanisms, we note that introducing Maxwell-Stefan drifting and Korteweg stress can qualitatively rationalize all major observations, although Korteweg stress's physical nature is still not well revealed. Decaying the nondilute effect under reducing Pe further supports the hypothesis.

Taking the significance of modeling CO_2 sequestration into consideration, we seriously call for attention from all relevant researchers to solve these problems. Our experiments, with rich details demonstrated and good reproducibility, could serve as a benchmark for future experimental and numerical approaches.

The data that support the findings of this study, the input files for simulation using CMG-STARS, MATLAB, and PYTHON source code used for experimental cloud diagrams; concentration distributions; and complex potential calculations in this study are publicly available through the Mendeley Data repository [53].

ACKNOWLEDGMENTS

We gratefully acknowledge the financial support and funding provided by the National Natural Science Foundation of China under Grant No. 12172010, and by the CNPC Research Institute of Petroleum Exploration and Development for the project "Key Fluid Mechanisms of CO_2 -EOR for Gu-Long Shale Oil Development." This work was supported by the National Natural Science Foundation of China (Grants No. 1217 and No. 2010).

F.Y. and Y.Z. undertook the experiments, numerical simulations, and original draft writing, that contributed to the work equally. S.Z. contributed in image data analysis. K.X. initiated the original idea, supervised this research, provided funding and revised the manuscript.

The authors have no conflict of interest to declare.

-
- [1] J. F. D. Tapia, J.-Y. Lee, R. E. H. Ooi, D. C. Y. Foo, and R. R. Tan, A review of optimization and decision-making models for the planning of CO_2 capture, utilization and storage (CCUS) systems, [Sustainable Prod. Consumption](#) **13**, 1 (2018).
 - [2] G. P. D. De Silva, P. G. Ranjith, and M. S. A. Perera, Geochemical aspects of CO_2 sequestration in deep saline aquifers: A review, [Fuel](#) **155**, 128 (2015).
 - [3] H. E. Huppert and J. A. Neufeld, The fluid mechanics of carbon dioxide sequestration, [Annu. Rev. Fluid Mech.](#) **46**, 255 (2014).
 - [4] B. Jha, L. Cueto-Felgueroso, and R. Juanes, Quantifying mixing in viscously unstable porous media flows, [Phys. Rev. E](#) **84**, 066312 (2011).
 - [5] M. A. Amooie, M. R. Soltanian, and J. Moortgat, Hydrothermodynamic mixing of fluids across phases in porous media, [Geophys. Res. Lett.](#) **44**, 3624 (2017).
 - [6] R. Farajzadeh, H. Salimi, P. L. J. Zitha, and H. Bruining, Numerical simulation of density-driven natural convection in porous media with application for CO_2 injection projects, [Int. J. Heat Mass Transfer](#) **50**, 5054 (2007).
 - [7] X. Zhou, Q. Yuan, Y. Zhang, H. Wang, F. Zeng, and L. Zhang, Performance evaluation of CO_2 flooding process in tight oil reservoir via experimental and numerical simulation studies, [Fuel](#) **236**, 730 (2019).

- [8] M. C. Kim, Effect of swelling on the onset of buoyancy-driven convection during the CO₂ dissolution process in a porous medium, *Int. J. Heat Mass Transfer* **100**, 779 (2016).
- [9] S. J. Watson, D. A. Barry, R. J. Schotting, and S. M. Hassanizadeh, Validation of classical density-dependent solute transport theory for stable, high-concentration-gradient brine displacements in coarse and medium sands, *Adv. Water Res.* **25**, 611 (2002).
- [10] J. Trémosa, C. Castillo, C. Q. Vong, C. Kervévan, A. Lassin, and P. Audigane, Long-term assessment of geochemical reactivity of CO₂ storage in highly saline aquifers: Application to Ketzin, In Salah and Snøhvit storage sites, *Int. J. Greenhouse Gas Control* **20**, 2 (2014).
- [11] Q. Fang, Y. Li, G. Peng, P. Cheng, and J. Lv, Effects of feldspar and salinity on the mineral sequestration capacity of CO₂ in high-salinity aquifers, *Environ. Earth Sci.* **75**, 1265 (2016).
- [12] Y. Tang, Z. Li, R. Wang, M. Cui, X. Wang, Z. Lun, and Y. Lu, Experimental study on the density-driven carbon dioxide convective diffusion in formation water at reservoir conditions, *ACS Omega* **4**, 11082 (2019).
- [13] H. R. Lashgari, A. Sun, T. Zhang, G. A. Pope, and L. W. Lake, Evaluation of carbon dioxide storage and miscible gas EOR in shale oil reservoirs, *Fuel* **241**, 1223 (2019).
- [14] P. Bikkina, J. Wan, Y. Kim, T. J. Kneafsey, and T. K. Tokunaga, Influence of wettability and permeability heterogeneity on miscible CO₂ flooding efficiency, *Fuel* **166**, 219 (2016).
- [15] Y. Song, N. Zhu, Y. Zhao, Y. Liu, L. Jiang, and T. Wang, Magnetic resonance imaging study on near miscible supercritical CO₂ flooding in porous media, *Phys. Fluids* **25**, 053301 (2013).
- [16] T. M. Weigand, P. B. Schultz, D. H. Giffen, M. W. Farthing, A. Crockett, C. T. Kelley, W. G. Gray, and C. T. Miller, Modeling nondilute species transport using the thermodynamically constrained averaging theory, *Water Resour. Res.* **54**, 6656 (2018).
- [17] W. Song, N. N. Ramesh, and A. R. Kovscek, Spontaneous fingering between miscible fluids, *Colloids Surf. A* **584**, 123943 (2020).
- [18] R. X. Suzuki, F. W. Quah, T. Ban, M. Mishra, and Y. Nagatsu, Experimental study of miscible viscous fingering with different effective interfacial tension, *AIP Adv.* **10**, 115219 (2020).
- [19] R. X. Suzuki, Y. Nagatsu, M. Mishra, and T. Ban, Phase separation effects on a partially miscible viscous fingering dynamics, *J. Fluid Mech.* **898**, A11 (2020).
- [20] V. A. Volpert, J. A. Pojman, and R. Texier-Picard, Convection induced by composition gradients in miscible systems, *C. R. Mec.* **330**, 353 (2002).
- [21] R. X. Suzuki, Y. Nagatsu, M. Mishra, and T. Ban, Fingering pattern induced by spinodal decomposition in hydrodynamically stable displacement in a partially miscible system, *Phys. Rev. Fluids* **4**, 104005 (2019).
- [22] S. M. Hassanizadeh, Derivation of basic equations of mass transport in porous media, Part 2. Generalized Darcy's and Fick's laws, *Adv. Water Res.* **9**, 207 (1986).
- [23] R. J. Schotting, H. Moser, and S. M. Hassanizadeh, High-concentration-gradient dispersion in porous media: Experiments, analysis and approximations, *Adv. Water Res.* **22**, 665 (1999).
- [24] T. M. Weigand and C. T. Miller, Microscale modeling of nondilute flow and transport in porous medium systems, *Phys. Rev. E* **102**, 033104 (2020).
- [25] A. Runstedtler, On the modified Stefan–Maxwell equation for isothermal multicomponent gaseous diffusion, *Chem. Eng. Sci.* **61**, 5021 (2006).
- [26] I. M. J. J. van de Ven-Lucassen, T. J. H. Vlught, A. J. J. van der Zanden, and P. J. A. M. Kerkhof, Molecular dynamics simulation of self-diffusion and maxwell-stefan diffusion coefficients in liquid mixtures of methanol and water, *Mol. Simul.* **23**, 79 (1999).
- [27] D. Truzzolillo and L. Cipelletti, Hydrodynamic instabilities in miscible fluids, *J. Phys.: Condens. Matter* **30**, 033001 (2018).
- [28] D. Truzzolillo and L. Cipelletti, Off-equilibrium surface tension in miscible fluids, *Soft Matter* **13**, 13 (2016).
- [29] E. N. Lightfoot, E. L. Cussler, and R. L. Rettig, Applicability of the Stefan-Maxwell equations to multicomponent diffusion in liquids, *AIChE J.* **8**, 708 (1962).
- [30] J. Pojman, Y. Chekanov, J. Masere, V. Volpert, T. Dumont, and H. Wilke, in *Proceedings of the 39th Aerospace Sciences Meeting and Exhibit (AIAA, Reston, VA, 2001)*.

- [31] I. Kostin, M. Marion, R. Texier-Picard, and V. A. Volpert, Modelling of miscible liquids with the Korteweg stress, *ESAIM: Math. Modell. Numer. Anal.* **37**, 741 (2003).
- [32] Y. Liu, Y. Teng, L. Jiang, J. Zhao, Y. Zhang, D. Wang, and Y. Song, Displacement front behavior of near miscible CO₂ flooding in decane saturated synthetic sandstone cores revealed by magnetic resonance imaging, *Magn. Reson. Imaging* **37**, 171 (2017).
- [33] G. Løvoll, Y. Méheust, R. Toussaint, J. Schmittbuhl, and K. J. Måløy, Growth activity during fingering in a porous Hele-Shaw cell, *Phys. Rev. E* **70**, 026301 (2004).
- [34] A. Marciales and T. Babadagli, Pore scale visual investigations on solvent retrieval during oil recovery at elevated temperatures: A micromodel study, *Chem. Eng. Res. Des.* **106**, 59 (2016).
- [35] E. M. Myshakin, H. Singh, S. Sanguinito, G. Bromhal, and A. L. Goodman, Flow regimes and storage efficiency of CO₂ injected into depleted shale reservoirs, *Fuel* **246**, 169 (2019).
- [36] S. Razi-perchikolaee, A. Pasumarti, and S. Mishra, The effect of natural fractures on CO₂ storage performance and oil recovery from CO₂ and WAG injection in an Appalachian basin reservoir, *Greenhouse Gases: Sci. Technol.* **10**, 1098 (2020).
- [37] Ø. Eide, M. A. Fernø, Z. Alcorn, and A. Graue, Visualization of carbon dioxide enhanced oil recovery by diffusion in fractured chalk, *SPE J.* **21**, 112 (2016).
- [38] D. A. De Mezquia, M. M. Bou-Ali, M. Larranaga, J. A. Madariaga, and C. Santamaria, Determination of molecular diffusion coefficient in *n*-alkane binary mixtures: Empirical correlations, *J. Phys. Chem. B* **116**, 2814 (2012).
- [39] See Supplemental Material at <http://link.aps.org/supplemental/10.1103/PhysRevFluids.8.044501> for technical details and extended discussions about micromodel fabrication, experimental setup, image analysis methods, operation details, validation of experimental reproducibility, etc., as noted in the maintext.
- [40] J. W. Grate, C. Zhang, T. W. Wietsma, M. G. Warner, N. C. Anheier, B. E. Bernacki, G. Orr, and M. Oostrom, A note on the visualization of wetting film structures and a nonwetting immiscible fluid in a pore network micromodel using a solvatochromic dye, *Water Resour. Res.* **46**, W11602 (2010).
- [41] Q. Wu, J. T. Ok, Y. Sun, S. T. Retterer, K. B. Neeves, X. Yin, B. Bai, and Y. Ma, Optic imaging of single and two-phase pressure-driven flows in nano-scale channels, *Lab Chip* **13**, 1165 (2013).
- [42] F. Serra and E. M. Terentjev, Nonlinear dynamics of absorption and photobleaching of dyes, *J. Chem. Phys.* **128**, 224510 (2008).
- [43] J. Oh, K.-Y. Kim, W. S. Han, T. Kim, J.-C. Kim, and E. Park, Experimental and numerical study on supercritical CO₂/brine transport in a fractured rock: Implications of mass transfer, capillary pressure and storage capacity, *Adv. Water Res.* **62**, 442 (2013).
- [44] C. F. Curtiss and R. B. Bird, Multicomponent diffusion in polymeric liquids, *Proc. Natl. Acad. Sci. USA* **93**, 7440 (1996).
- [45] J. A. Pojman, Y. Chekanov, V. Wyatt, N. Bessonov, and V. Volpert, Numerical simulations of convection induced by Korteweg stresses in a miscible polymer–monomer system: Effects of variable transport coefficients, polymerization rate and volume changes, *Microgravity Sci. Technol.* **21**, 225 (2008).
- [46] D. A. Bratsun and A. De Wit, On Marangoni convective patterns driven by an exothermic chemical reaction in two-layer systems, *Phys. Fluids* **16**, 1082 (2004).
- [47] S. Berg, Marangoni-driven spreading along liquid-liquid interfaces, *Phys. Fluids* **21**, 032105 (2009).
- [48] A. VorobeV, Dissolution dynamics of miscible liquid/liquid interfaces, *Curr. Opin. Colloid Interface Sci.* **19**, 300 (2014).
- [49] N. Bessonov, V. A. Volpert, J. A. Pojman, and B. D. Zoltowski, Numerical simulations of convection induced by Korteweg stresses in miscible polymermonomer systems, *Microgravity Sci. Technol.* **17**, 8 (2005).
- [50] B. Wei, H. Gao, W. Pu, F. Zhao, Y. Li, F. Jin, L. Sun, and K. Li, Interactions and phase behaviors between oleic phase and CO₂ from swelling to miscibility in CO₂-based enhanced oil recovery (EOR) process: A comprehensive visualization study, *J. Mol. Liq.* **232**, 277 (2017).

- [51] M. Singh, A. Chaudhuri, P. H. Stauffer, and R. J. Pawar, Simulation of gravitational instability and thermo-solutal convection during the dissolution of CO₂ in deep storage reservoirs, *Water Resour. Res.* **56**, e2019WR026126 (2020).
- [52] Z. Dai *et al.*, Reactive chemical transport simulations of geologic carbon sequestration: Methods and applications, *Earth Sci. Rev.* **208**, 103265 (2020).
- [53] <https://data.mendeley.com/drafts/kzwmtrwjpt>.